

RESEARCH ARTICLE

10.1002/2016JC012164

Isopycnal eddy mixing across the Kuroshio Extension: Stable versus unstable states in an eddying model

Ru Chen¹ , Sarah T. Gille¹ , and Julie L. McClean¹ ¹Scripps Institution of Oceanography, University of California, San Diego, La Jolla, California

Key Points:

- Cross-jet eddy mixing was compared for the stable and unstable states of the Kuroshio Extension
- Mixing has significant spatiotemporal variability: both mean flow and eddies differ between the two states
- Eddy mixing coefficients in coarse-resolution models should have spatiotemporal variations

Correspondence to:

R. Chen,
ruchen@alum.mit.edu

Citation:

Chen, R., S. T. Gille, and J. L. McClean (2017), Isopycnal eddy mixing across the Kuroshio Extension: Stable versus unstable states in an eddying model, *J. Geophys. Res. Oceans*, 122, 4329–4345, doi:10.1002/2016JC012164.

Received 19 JUL 2016

Accepted 18 APR 2017

Accepted article online 24 APR 2017

Published online 24 MAY 2017

Abstract The Kuroshio Extension (KE) jet transitions between stable and unstable states on interannual time scales. Cross-jet eddy mixing in the two states is contrasted in the KE region (28°–40°N, 125°–165°E), using a global eddying 0.1° configuration of the Parallel Ocean Program with online numerical particles. The 4 year period chosen (June 1994 to May 1998) covers a full cycle of the stable state, unstable state and the transition period. Large values of cross-jet eddy diffusivities within the KE jet are concentrated in the upper 1000 m. In the upper ocean, elevated cross-jet mixing within the KE jet is mainly concentrated in the downstream part of the KE jet, where the jet is weak but eddy activity is strong. The simulated time-mean KE jet is more intense and extends further east in the stable state than in the unstable state. Consequently, strong cross-jet mixing within the KE jet is located west of 150°E during June 1996 to May 1997 (a typical unstable state), but east of 150°E during June 1995 to May 1996 (a typical stable state). However, average mixing within the KE jet is indistinguishable in the typical stable and unstable states. In the deep ocean, mixing is strongly influenced by topography, and thus their horizontal structures have less inter-annual variability than in the upper ocean. One caveat is that results here cover one representative cycle of the two states. To obtain the climate mean mixing structures for the stable or unstable state, one would need numerical output covering a period much longer than 4 years.

1. Introduction

The Kuroshio Extension (KE) is the eastward extension of the northward flowing western boundary current in the North Pacific. It is intense in magnitude and is characterized by strong meanders and pinched off mesoscale vortices. This strongly inertial jet creates a front between the subtropical and subpolar gyres, and eddies contribute greatly to the cross-frontal fluxes of tracers (e.g., heat, salt, carbon) and thus to the North Pacific climate [e.g., Donohue *et al.*, 2008]. Consequently, much effort has been directed toward understanding the importance of eddies in the KE, for example, through the recent observational Kuroshio Extension System Study (KESS) field campaign [e.g., Donohue *et al.*, 2008]. Processes studied during KESS include the vertical coupling of the KE and deep-ocean eddies [Greene *et al.*, 2009, 2012], eddy-mean flow interaction [Waterman *et al.*, 2011], propagation of KE meanders [Tracey *et al.*, 2012], and the mean structures and spatiotemporal variability of divergent eddy heat fluxes [Bishop *et al.*, 2013; Bishop, 2013].

Sea surface height (SSH) observations reveal that the mean flow and eddies that comprise the KE system oscillate between a stable state and an unstable state on interannual time scales [e.g., Qiu, 2003; Qiu and Chen, 2010; Qiu *et al.*, 2014a]. In the stable state, the KE jet is intense and elongated, producing strong inertial eastward transport and low eddy activity, while in the unstable state, the KE jet is weak and contracted, with rich eddy activity [e.g., Qiu and Chen, 2010]. While the cause of the two states remains an active research area, decadal variability of wind stress curl forcing in the central Pacific and westward propagating Rossby waves have been proposed as mechanisms responsible for their occurrences [e.g., Qiu, 2003; Qiu *et al.*, 2014a]. The impacts of decadal variability of the KE state on meridional heat transport, winter time sea surface temperature, and the properties of water masses, particularly North Pacific Intermediate Water, have also been investigated [e.g., Qiu and Miao, 2000; Qiu and Chen, 2011; Bishop *et al.*, 2015]. The two states of the KE also have significant impact on surface chlorophyll concentration in the KE region [Lin *et al.*, 2014] and on the atmospheric circulation in the Northern Hemisphere [e.g., Révelard *et al.*, 2016; O'Reilly and Czaja, 2015].

The role of the two KE states in cross-jet mixing, however, remains unclear. Mixing across the KE jet controls the exchange of water masses between the subpolar and subtropical gyres, impacting water mass

composition and thus North Pacific climate [e.g., Qiu *et al.*, 2007; Donohue *et al.*, 2008; Qiu and Chen, 2011; Oka and Qiu, 2012]. Hence, differences in cross-jet mixing during the two KE states could have ramifications for climate. Recent work suggests that both eddies and jet properties can influence cross-jet mixing processes [e.g., Ferrari and Nikurashin, 2010; Chen *et al.*, 2014, 2015]. For example, the propagation of eddies relative to the mean flow can lead to the suppression of mixing across the jet in oceanic regions with intense jets but away from topography [e.g., Chen *et al.*, 2014]. Because the two states of the KE are characterized by different jet structures and eddy kinetic energy levels, we initially hypothesized that mixing and transport of key climate tracers across the jet (e.g., heat, salt, carbon, potential vorticity, etc.) would also have strong interannual variability.

Our focus here is not to explain the origin of the complex temporal variability, but to characterize the consequences of the two states for mixing. We aim to estimate eddy mixing across the jet in both stable and unstable states and to assess the role of the two states in mixing structures. To our knowledge, isopycnal mixing in the KE region has rarely been explored. One exception is Chen *et al.* [2014], who characterized the three-dimensional spatial structures of eddy diffusivities in the KE region from a strongly eddying ocean general circulation model (OGCM) and interpreted the spatial structures using existing mixing theories (e.g., critical layer theory from Green [1970]). In the present study, instead of diagnosing the full eddy diffusivity tensor, we focus on cross-stream diffusivities, the component of eddy diffusivity that is perpendicular to the mean flow.

In contrast to the limited number of mixing studies in the KE region, in the Southern Ocean there has been a profusion of recent mixing investigations, many related to the Diapycnal and Isopycnal Mixing Experiment in the Southern Ocean (DIMES) [Gille *et al.*, 2012]. The field experiment was motivated by the close link between mixing and the meridional overturning circulation [e.g., Danabasoglu and Marshall, 2007; Ito and Marshall, 2008]. The spatial patterns and magnitudes of eddy diffusivities have been estimated in the Southern Ocean using observations and models [e.g., Abernathey *et al.*, 2010; Griesel *et al.*, 2010, 2014; LaCasce *et al.*, 2014; Lu *et al.*, 2016; Boland *et al.*, 2015]. Theoretical progress has also been made toward understanding the cross-jet mixing suppression induced by the propagation of eddies relative to the mean flow [e.g., Ferrari and Nikurashin, 2010; Abernathey *et al.*, 2010; Klocker *et al.*, 2012a; Bates *et al.*, 2014; Chen *et al.*, 2015], which was originally introduced by Green [1970].

In this work, we aim to contrast cross-jet mixing in examples of unstable and stable states of the KE region. The KE and the Antarctic Circumpolar Current are visually similar in that both current systems are energetic and have intense jets. We could apply the mixing diagnosis methods, theories and insights that were developed for the ACC, as summarized above, to the KE region. In this work, we focus on estimating eddy diffusivities using a diagnostic approach based on numerical floats advected on-line in a strongly eddy-active ocean general circulation model (OGCM). This approach has been successfully used in previous mixing studies in both the Southern Ocean and Kuroshio Extension regions [e.g., Griesel *et al.*, 2014; Chen *et al.*, 2014, 2015].

This paper is organized as follows. Section 2 introduces the global OGCM model and the float-based method used to diagnose eddy diffusivities in the cross-mean flow direction. Section 3 characterizes the stable and unstable states in the global eddying model and compares them with their observation counterparts. Section 4 presents the spatial structures and magnitude of cross-stream eddy diffusivities in both stable and unstable states. Section 5 provides a summary.

2. Numerical Model and Methodology

2.1. Model Setup and Float Deployment

We use the Parallel Ocean Program (POP), a global eddying model with a nominal resolution of 0.1° and 42 vertical levels [Dukowicz and Smith, 1994]. This model has the capability to advect numerical floats online and has been used to infer eddy diffusivities [e.g., Griesel *et al.*, 2014]. The detailed configuration of the numerical model (e.g., subgrid parameterizations, initial state, atmospheric forcing) has been described in several mixing studies [e.g., Chen *et al.*, 2014, 2015; Griesel *et al.*, 2014, 2015]. Post-spin-up Eulerian output is available for the period 1994–2007; these output fields are used to provide initial conditions for our float experiments.

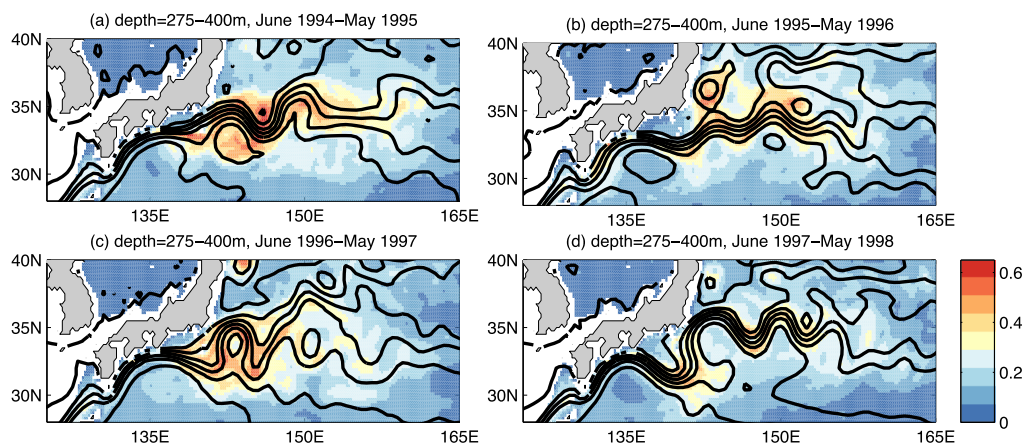


Figure 1. Time-mean eddy velocity magnitude (m s^{-1} , in color) at 275–400 m during the time period (a) June 1994 to May 1995, (b) June 1995 to May 1996, (c) June 1996 to May 1997 and (d) June 1997 to May 1998. Black contours are barotropic streamlines ψ_g , defined in equation (1). Here eddy velocity, (u', v') , is defined as the deviation of the total velocity, (u, v) , from the time-mean velocity over the selected time period, (\bar{u}, \bar{v}) . In other words, $u' = u - \bar{u}$ and $v' = v - \bar{v}$.

To compare cross-jet mixing between the stable and unstable states, four numerical experiments are conducted. In Experiment 1, numerical floats are deployed globally in June 1994 and are advected by the three-dimensional velocity field for 18 months. A fourth-order Runge-Kutta scheme is employed to advect the online floats. As described by *Chen et al.* [2014], these particles are deployed globally at 0.25° meridional resolution, 2.5° zonal resolution and at 23 vertical levels. The depth of the particle deployment follows the natural vertical discretization of the POP model. Specifically, particles are deployed at 11 levels in the upper 1000 m, eight levels between 1000 and 3000 m and four levels below 3000 m. Experiments 2, 3, and 4 use the same setup as Experiment 1, except that the floats are deployed in June 1995, June 1996, and June 1997, respectively.

To fully resolve the interannual variability of eddy mixing in the KE region, one would ideally extend the experiments to encompass the full 14 year period (1994–2007) of output that is available from the POP model simulation. However, numerical experiments with floats are computationally expensive. Our choice of four experiments is a compromise intended to make efficient use of computing resources in order to resolve one oscillation cycle (stable state, unstable state and the transition between states).

The period we have selected (June 1994 through May 1998) is long enough to capture a typical stable and a typical unstable state. Figures 1 and 2 respectively show the time-mean of eddy velocity magnitude and

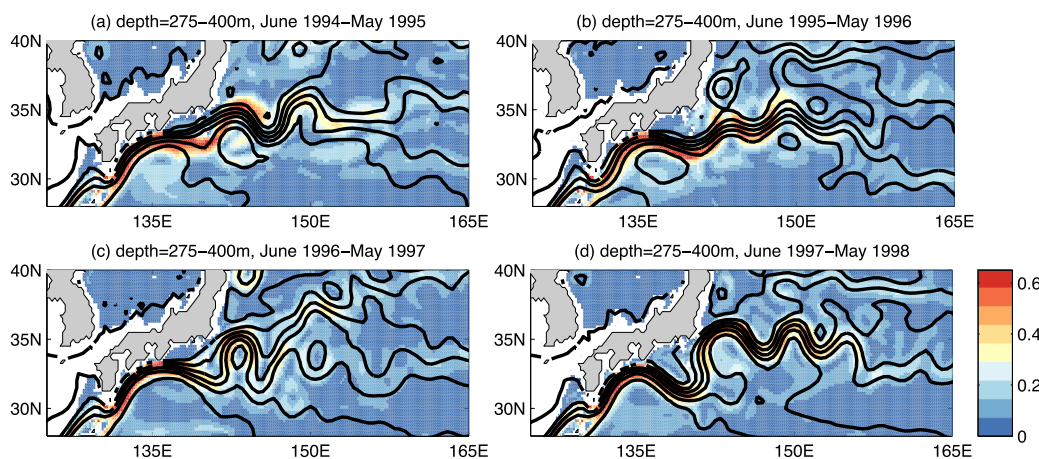


Figure 2. The magnitude of time-mean velocity (m s^{-1} , in color) at 275–400 m during the time period (a) June 1994 to May 1995, (b) June 1995 to May 1996, (c) June 1996 to May 1997 and (d) June 1997 to May 1998. Black contours are barotropic streamlines ψ_g , defined in equation (1).

the magnitude of the mean flow at 275–400 m in each of the 4 year periods. Here the velocity of the mean flow, (\bar{u}, \bar{v}) , is defined as the time-mean velocity over each 1 year period (e.g., June 1994 to May 1995) and eddy velocity, (u', v') is defined as the deviation of total velocity from the mean flow velocity. Thus, eddy velocity magnitude, $\sqrt{u'^2 + v'^2}$, is just $\sqrt{(u - \bar{u})^2 + (v - \bar{v})^2}$.

The annual mean barotropic streamlines in each of the 4 year periods are imposed on Figures 1 and 2. The barotropic streamline is approximated as

$$\psi_g = gf^{-1}\eta, \tag{1}$$

with g denoting gravity, f the Coriolis parameter and η the time-mean SSH in each period. These streamlines indicate the location of the time-mean KE jet as well as the jet strength, though the jet strength can also be revealed from the mean flow magnitude in Figure 2. Strong temporal variability exists during the model run. For example, in period 2 (June 1995 to May 1996), the KE jet is intense and extends east of 150°E (Figure 2), and the eddy velocity magnitude is relatively low compared to period 1 (June 1994 to May 1995) or period 3 (June 1996 to May 1997) (Figure 1). In period 2, the KE jet is in a typical stable state, with intense zonal transport and relatively weak eddy activity (Figures 1b and 2b). Period 3 (June 1996 to May 1997) represents a typical unstable state, with a contracted KE jet and rich eddy activity: the KE jet is greatly weakened once it reaches 140°E but the eddy velocity magnitude is relatively large (Figures 1c and 2c). Periods 1 and 4 are neither stable nor unstable: in period 1, the KE jet is intense, but eddy activity is rich, whereas in period 4 (June 1997 to May 1998), the KE jet is also intense, but has a large meandering structure south of the Japan coast compared to period 2 (Figures 1a, 1d, 2a, and 2d). This deep meander path south of the Japan coast has been studied extensively, and its generation and decay have been related to internal oscillations, the velocity and position of the Kuroshio Current in the Tokara Strait south of Kyushu, and meso-scale eddies in the subtropical gyre [e.g., Kawabe, 1986; Qiu and Miao, 2000; Miyazawa et al., 2004]. To contrast different time periods, we estimated diffusivities over periods 1–4. Diagnosis methods are described in section 2.2.

2.2. Methods to Estimate Cross-Stream Eddy Diffusivities

Diagnostic methods that have been used extensively in earlier mixing studies include those that have explored Nakamura effective diffusivities [e.g., Marshall et al., 2006], diffusivities based on flux-gradient relationships [e.g., Bachman and Fox-Kemper, 2013], and particle-based diffusivities [e.g., LaCasce and Bower, 2000; Chen et al., 2014; Wolfram et al., 2015]. We estimate single-particle cross-stream diffusivities, taking advantage of a diagnostic framework which originated from Davis [1987, 1991] and has been justified in previous work [e.g., Oh et al., 2000; Zhurbas and Oh, 2003, 2004; Katsumata and Yoshinari, 2010; Qian et al., 2013; Chiswell, 2013; Chen et al., 2014, 2015; Griesel et al., 2014, 2015].

Specifically, the diagnostic formula we employ is

$$\kappa_{\perp}^{\infty}[\mathbf{x}, (T_1, T_2)] = \lim_{\tau \rightarrow \infty} \kappa_{\perp}[\mathbf{x}, \tau, (T_1, T_2)] = \lim_{\tau \rightarrow \infty} \int_0^{\tau} d\tilde{\tau} \langle u'_{\perp}(t_0 | \mathbf{x}, t_0) u'_{\perp}(t_0 + \tilde{\tau} | \mathbf{x}, t_0) \rangle_{L, [T_1, T_2]}, \tag{2}$$

where $\kappa_{\perp}^{\infty}[\mathbf{x}, (T_1, T_2)]$ denotes the cross-stream eddy diffusivities in a bin with the centroid \mathbf{x} over a selected period $[T_1, T_2]$. Consistently, $\langle \cdot \rangle_{L, [T_1, T_2]}$ denotes the ensemble average of floats passing through a bin with centroid \mathbf{x} and over the period $[T_1, T_2]$. The term τ denotes the time lag, which can be either positive or negative. As described by Chen et al. [2014], $u'_{\perp}(t | \mathbf{x}, t_0)$ denotes the residual velocity in the direction perpendicular to the “mean flow” at time t , for the float passing position \mathbf{x} at time t_0 . In this work, “mean flow” denotes the temporal average of the Eulerian velocity over the period $[T_1, T_2]$ at the float position at time t . Residual velocity at time t for a selected float is the difference between the total velocity of the float at time t and the mean flow at the float position at time t . Therefore, cross-stream diffusivities here do not include the contribution of the time-mean flow and its shear to mixing and dispersion. Henceforth “diffusivities” or “eddy-diffusivities” are often used to denote “cross-stream diffusivities”.

In practice, since we cannot advect floats for an infinite time period, the maximum value of τ in equation (3) cannot be infinity. As τ increases, the residual velocity decorrelates from that at $\tau = 0$ and thus $\kappa_{\perp}[\mathbf{x}, \tau, (T_1, T_2)]$ asymptotes to constant values. In other words, $\kappa_{\perp}[\mathbf{x}, \tau, (T_1, T_2)]$ generally levels off, i.e., converges to a

constant value, as τ increases to a certain value τ_1 . Therefore, $\kappa_{\perp}^{\infty}[\mathbf{x}, (T_1, T_2)]$ presented in section 4 is approximated by

$$\kappa_{\perp}^{\infty}[\mathbf{x}, (T_1, T_2)] = \lim_{\tau \rightarrow \infty} \kappa_{\perp}[\mathbf{x}, \tau, (T_1, T_2)] \approx \frac{\int_{\tau_1}^{\tau_2} \kappa_{\perp}[\mathbf{x}, \tilde{\tau}, (T_1, T_2)] d\tilde{\tau} + \int_{-\tau_2}^{-\tau_1} \kappa_{\perp}[\mathbf{x}, \tilde{\tau}, (T_1, T_2)] d\tilde{\tau}}{2(\tau_2 - \tau_1)}. \quad (3)$$

In most bins, $\kappa_{\perp}[\mathbf{x}, \tau, (T_1, T_2)]$ levels off as τ approaches 50 days. Thus, we chose τ_1 to be 50 days. The maximum τ here is 69 days, and thus we take $[\tau_1, \tau_2]$ to be [50, 69] days. The criteria to test the convergence of $\kappa_{\perp}[\mathbf{x}, \tau, (T_1, T_2)]$ are presented in the appendix of *Chen et al.* [2014].

Following *Chen et al.* [2014], we use the adaptive bin approach and pseudo tracks to estimate diffusivities. First, pseudo float tracks are generated from the float trajectories during the selected period $[T_1, T_2]$. As described in *Chen et al.* [2014], we gather the float positions every other day and then “track” the identified float forward and backward for 69 days. Note that the output of these numerical floats (e.g., positions, velocity), advected online by the full velocity fields, is saved at daily intervals, and thus in this context “tracking” means extracting the corresponding positions of the identified float at daily intervals. Then, the positions of the floats at each pseudo track at the center time, i.e., $\tau = 0$, are used to divide the entire study domain into adaptive bins following the clustering approach of *Koszalka and LaCasce* [2010]. In contrast with regular geographic bins, adaptive bins are irregular in shape and size, and are irregularly distributed in space (dots in Figure 3a). However, the number of pseudo tracks in each adaptive bin is roughly uniform throughout the study domain, leading to improved convergence properties (Figure 3b). Were we to use regular geographic bins, the number of float days in each bin would be highly spatially inhomogeneous, despite the uniform deployment of floats, due to the inhomogeneity of oceanic motions (e.g., color in Figure 3a). By using adaptive bins, we obtain diffusivity estimates that converge relatively consistently and with uniform uncertainties compared with what we would obtain from geographic bins [*Koszalka and LaCasce*, 2010; *Chen et al.*, 2014]. To estimate the diffusivity error bars, we chose to use a bootstrapping technique, which has been widely employed in previous studies of eddy diffusivities [e.g., *Griesel et al.*, 2010; *Klocker et al.*, 2012b; *Chen et al.*, 2014; *Roach et al.*, 2016] and dissipation rate [e.g., *Holmes et al.*, 2016; *Merrifield et al.*, 2016]. Details of the convergence test and bootstrapping technique are described by *Chen et al.* [2014]. In section 4, $\kappa_{\perp}[\mathbf{x}, \tau, (T_1, T_2)]$ values, which have not converged over $[\tau_1, \tau_2]$ or $[-\tau_2, -\tau_1]$, are not presented. To aim for an equal number of float days in each depth range, we divide the upper 3900 m into 11 nonoverlapping depth ranges for the diffusivity estimates.

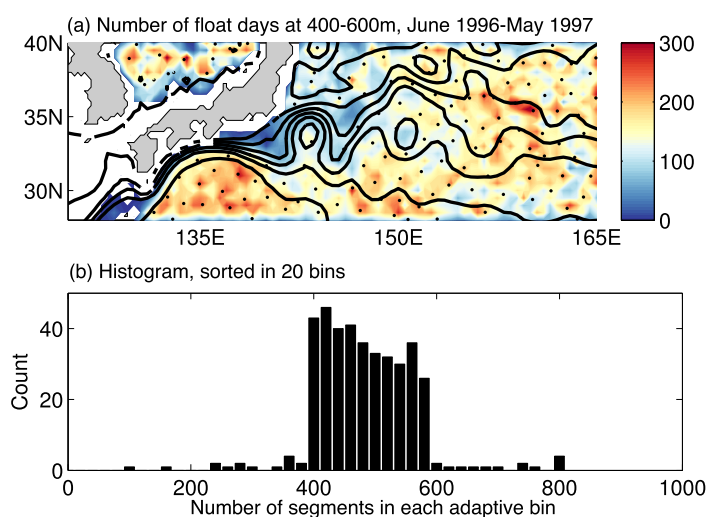


Figure 3. (a) The number of days that numerical particles spent in each $0.5^{\circ} \times 0.5^{\circ}$ geographic bin at the depth range of 400–600 m during June 1996 to May 1997 (color). The black dots show the location of the centroids of each adaptive bin. Black contours are barotropic streamlines ψ_g defined in equation (1). (b) Histogram of the number of pseudo tracks in each adaptive bin at 400–600 m.

3. Model-Data Comparison

In this section, we assess whether the two dynamical states of the KE identified from observations [e.g., *Qiu and Chen*, 2010; *Qiu et al.*, 2014a] also exist in the POP model and evaluate how well they resemble the observed states from a statistical perspective. We will show that the POP model captures the two dynamical states realistically, and our simulation period is representative of a full oscillation cycle as seen in the observations.

3.1. Satellite Observations

Earlier studies have typically used SSH observations to separate the temporally varying KE

structures into two dynamical states [e.g., *Qiu and Chen*, 2010]. Likewise, we use gridded absolute dynamic topography, computed in delayed mode from all available satellite altimeters and distributed by Archiving Validation and Interpretation of Satellite Data in Oceanography (AVISO) (<http://www.aviso.altimetry.fr/>). These altimeter-derived data are released on a 0.25° spatial grid. We compare Eulerian model output and SSH data over the entire 14 years of the model simulation (1994–2007), instead of the 4 year time period with floats (June 1994 to May 1998), to obtain more reliable statistics.

Although satellite observations do not resolve variability on daily time scales, the AVISO data have been interpolated to daily intervals. To be consistent, the model-data comparisons shown below are based on the daily-averaged POP model output interpolated onto the grid of the AVISO observations. Model-data comparisons based on weekly averaged POP output (not shown) closely match those based on daily output presented in section 3.3. Though the particle trajectories are advected online in our numerical experiments, our mixing results (section 4) are diagnosed from particle velocities saved at daily intervals.

3.2. Metrics for Model-Data Comparison

Metrics often used to separate the unstable state from the stable state include the length and position of KE paths and eddy kinetic energy [e.g., *Qiu and Chen*, 2005, 2010]. AVISO observations of the KE paths (position and length) and surface geostrophic EKE suggest that, compared to the unstable state, the KE jet in the stable state is intense, its position is further north, and the path length is small due to relatively less eddy activity [*Qiu and Chen*, 2010]. In the unstable state, the KE path is weak, the path position is further south, and strong eddy activity leads to large path lengths [*Qiu and Chen*, 2010].

The KE jet is a major geostrophic current with a strong zonal component of volume transport, so it should correspond to a strong meridional gradient in SSH. *Qiu and Chen* [2010] defined the KE path by the fixed SSH contour that is located closest to the largest meridional gradient in SSH [see also *Bishop et al.*, 2015]. As an alternative, *Delman et al.* [2015] proposed a “steepest gradient” method, which allows the selected SSH contour to have time-dependent values and aims to get the closest match between the identified KE path and the largest SSH gradient. However, in this study, we use the simpler fixed SSH contour approach [e.g., *Qiu and Chen*, 2010], in order to be consistent with most previous studies of the KE’s two states. In the POP model, we found that the KE paths identified from the “steepest gradient” method are not smooth and have abrupt meridional changes in position.

We define the 70 cm SSH contour in the POP model and the 110 cm SSH contour in the AVISO data as the KE path, similar to the values used by *Bishop et al.* [2015]. In both cases, these SSH contours are geographically near the largest meridional gradient in SSH. Note that the SSH contour corresponding to the KE path in the POP model differs from that in AVISO data, and this difference is consistent with the model-data difference of the SSH reference level. In some SSH snapshots, the SSH contour not only identifies the KE path, but also marks closed vortices. These vortices were not treated as part of the KE jet, and they were not taken into account when calculating path lengths and path positions.

3.3. Results

Figure 4 shows the time series of path position, path length and geostrophic EKE in the region 141°–153°E, 32°–38°N. Note that different studies have used different longitudinal ranges to define the KE area when evaluating jet path properties [e.g., *Qiu and Chen*, 2005, 2010, 2011; *Douglass et al.*, 2012; *Bishop et al.*, 2015]. Here we use the region most commonly examined in the literature: 141°–153°E, 32°–38°N, where eddy activity is very strong. The geostrophic EKE is defined as

$$EKE_{geo} = (u'_{geo}{}^2 + v'_{geo}{}^2) / 2, \tag{4}$$

where u'_{geo} and v'_{geo} are the anomalies of zonal and meridional geostrophic velocities at the ocean surface. These geostrophic velocities can be inferred from SSH using the geostrophic relation, and anomalies are computed as deviations from the time mean.

The path properties and geostrophic EKE are similar in POP and in observations, in that both show strong interannual variability with similar magnitudes (Figure 4). The POP model represents the variability of the path position, including the southward path positions before 1996, its northward positions during 1997–2000, and the small fluctuations during 2000–2006 (Figure 4). The model also captures positive anomalies in path length and EKE during 1998–2002. However, before 1996, the EKE level in the POP model is higher

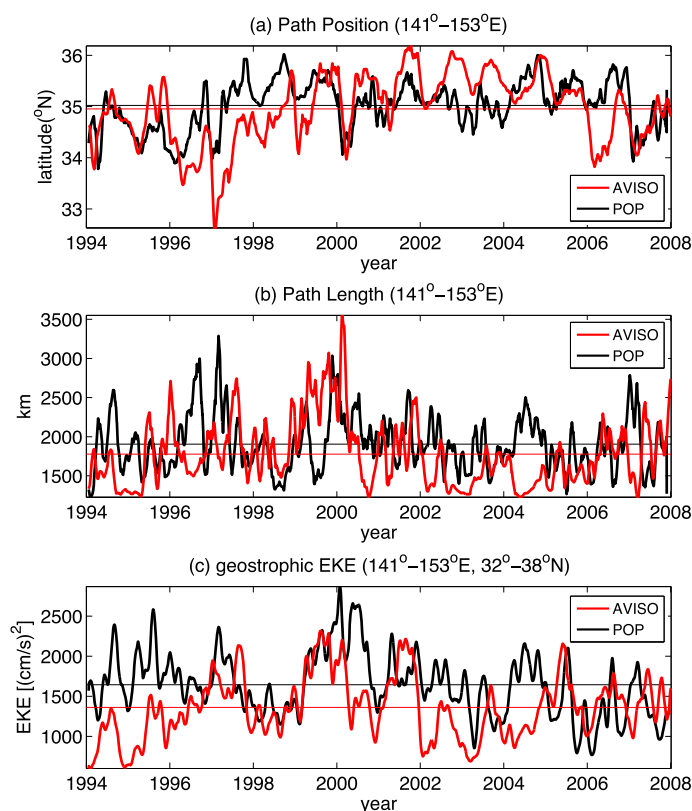


Figure 4. (a) The mean meridional position of the Kuroshio Extension path as a function of time from daily AVISO (red) and daily POP (black) in the longitude range 141° – 153° E. (b) Same as Figure 4a, but for the path length. (c) The geostrophic EKE, defined by equation (4), averaged over the region 141° – 153° E, 32° – 38° N from POP (black) and AVISO (red). The KE path is defined in section 3.2. The time series shown here are the 30 day running averages of the daily time series. The horizontal lines in Figures 4a–4c are the time mean of the time series of the same color.

to the fact that the gridded AVISO product does not resolve oceanic eddy motions with scales smaller than 150 km [Chelton *et al.*, 2011].

To evaluate whether the POP model correctly captures the magnitude of the temporal variability at resolved time scales, we diagnosed the power spectra of path position (Figure 5a), path length (Figure 5b) and geostrophic EKE (Figure 5c). Both the magnitude and slope of the POP spectra are roughly consistent with their observed counterparts (Figure 5). However, compared with POP, the geostrophic EKE spectrum from AVISO has slightly smaller values at the 5–20 day period (Figure 5c), which could be due to the coarse temporal resolution of the satellite data.

Here we use path length as the index to distinguish between stable and unstable states. The stable state corresponds to a small path length, i.e., negative path length anomalies, and the unstable state corresponds to a large path length, i.e., positive path length anomalies. Using this criterion, we conclude that, in the POP model, the KE jet is in a typical unstable state in period 3 and is in a typical stable state in period 2 (Figure 4b). The path length in periods 1 and 4 has both positive and negative anomalies, and thus the KE jet states in these two periods are not typically stable or unstable.

The timing of the two states differs in POP and in observations (Figure 4). For example, in the year 2004, the KE jet in the POP model is in an unstable state corresponding to positive path length anomalies, but the observed KE jet is in a stable state corresponding to negative path length anomalies (Figure 4b). The correlation coefficients between observed and modeled path length, path positions and geostrophic EKE are 0.23 ± 0.03 , 0.05 ± 0.03 and 0.32 ± 0.02 , respectively. The error bars are uncertainties of correlation coefficients at the 95% confidence level. The low correlations found here are consistent with the model-data difference in the timing of the two states. This timing difference is not surprising, as the KE variability is due to

than in observations, though its fluctuation characteristics agree with observations (Figure 4). The KE path in the POP model is prematurely northward in 1997–1999 relative to the observed KE path. The path lengths in the years 1994, 1996–1997, and 2004 have positive anomalies in the POP model, but not in observations.

The time-mean geostrophic EKE in POP is larger than in AVISO in the region 141° – 153° E, 32° – 38° N (horizontal lines in Figure 4c). To diagnose the reason for these EKE differences, we examined one-dimensional EKE wavenumber spectra for POP and AVISO (not shown). For spatial scales smaller than 75 km, POP spectra are statistically significantly more energetic than AVISO spectra (at the 95% confidence level), which accounts for the differences in the time mean geostrophic EKE. This difference in geostrophic EKE between high-resolution ocean models and the AVISO product has also been identified by Qiu *et al.* [2014b], who attributed it

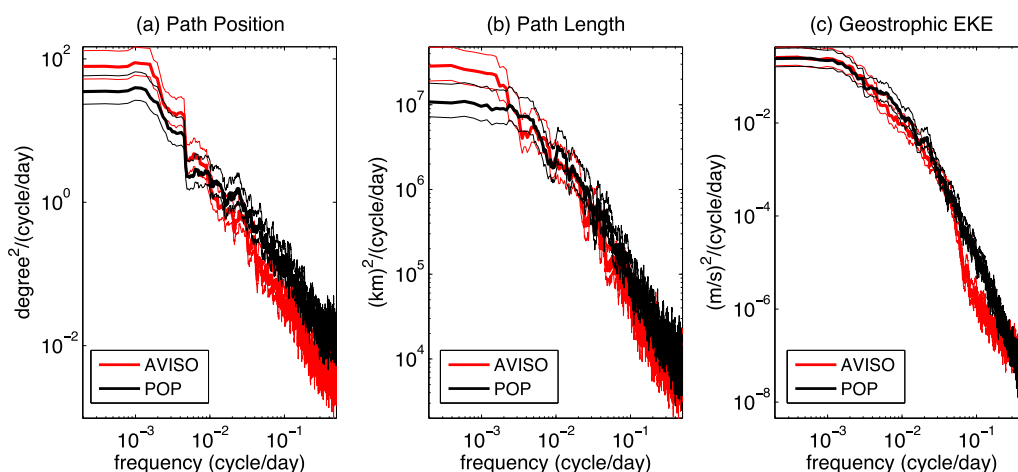


Figure 5. (a) The frequency spectra of the meridional position of the Kuroshio Extension jet path in the longitude range $141^{\circ} - 153^{\circ}\text{E}$; (b) same as Figure 5a, but for the path length; (c) the frequency spectra of the geostrophic EKE averaged over the region $141^{\circ} - 153^{\circ}\text{E}$, $32^{\circ} - 38^{\circ}\text{N}$. Thick solid lines show the spectra and thin solid line indicates the 95% confidence limits. Demeaned daily time series are used, and spectra are computed using the multitaper spectral method.

a combination of atmospheric forcing variability and intrinsic variability due to nonlinearity (e.g., eddy-eddy interaction, baroclinic instability). The latter is hard to simulate or predict due to the turbulent nature of the oceanic circulation.

To summarize, the POP model statistically represents the two-states reasonably well, in particular the amplitude of temporal variability. However, part of the KE variability is due to intrinsic variability, which is hard to simulate at the same time as occurs in the observations, leading to the model-data differences in the timing of the two states. Note that previous studies also have demonstrated that the POP model is an effective tool to evaluate the KE path fluctuations [e.g., Douglass *et al.*, 2012], KE dynamics [e.g., Delman *et al.*, 2015] and eddy mixing [e.g., Chen *et al.*, 2014, 2015; Griesel *et al.*, 2014, 2015].

4. Mixing in Stable and Unstable States

This section characterizes the interannual variability of cross-stream eddy diffusivities from POP, with particular emphasis on how their spatial structures and total mixing rates vary from year to year.

4.1. Horizontal Structures: Combination Effect of Mean Flow and Eddies

4.1.1. Upper Ocean

POP diffusivities in the upper ocean have strong interannual variability (Figure 6). Red shading in Figure 6 indicates elevated mixing. In period 1, during which a strong jet extends eastward to around 150°E , elevated mixing occurs within the recirculation gyre region located to the south of the jet and west of 150°E . Mixing inside the weak jet east of 150°E is also larger than in the ambient surroundings. In period 2, mixing is large north of the intense jet located west of 150°E , and it is also large inside the jet east of 150°E . During period 3, the KE jet is greatly weakened immediately after the jet leaves the Japanese coast, and mixing is elevated inside the weakened jet. During period 4, diffusivities north of 30°N are smaller than in other periods due to the low eddy activity in period 4. Results at 400–900 m (not shown) are similar to those at 275–400 m shown in Figure 6.

Negative diffusivities also occur within the KE jet, in particular west of the Izu Ridge and near 151°E (Figure 6). These negative values have also been identified in previous KE studies [e.g., Chen *et al.*, 2014], and are associated with upgradient eddy fluxes. Detailed mechanisms for upgradient eddy fluxes in the downstream KE region have been discussed by Waterman and Jayne [2011] and Waterman *et al.* [2011].

The complex spatiotemporal structures of diffusivities in the upper ocean, such as those shown in Figure 6, are to a large extent controlled by both the mean flow and eddies. The squeezing of the barotropic streamlines in Figure 6 corresponds to a strong KE jet, and the divergent streamlines correspond to a weak KE jet. Although eddy velocity magnitudes are largest within the KE jet (Figure 1), mixing is generally small within

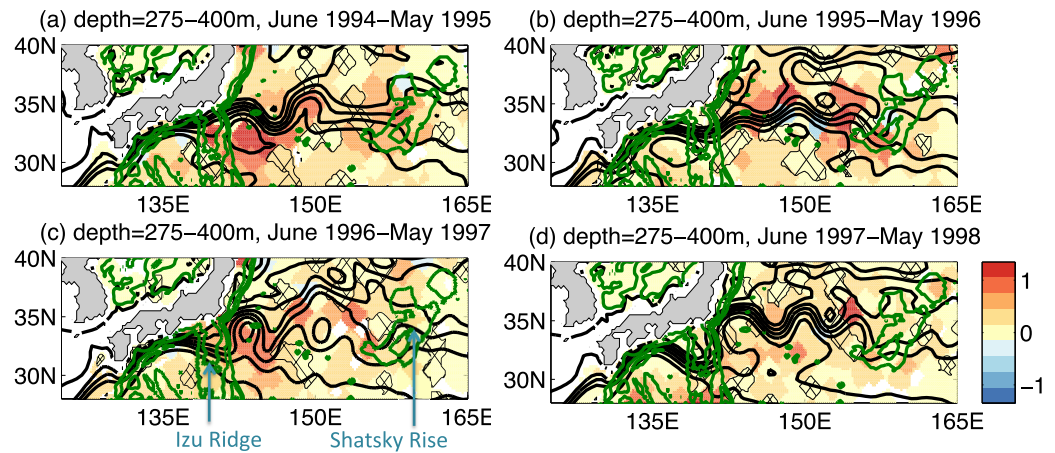


Figure 6. Time-mean cross-stream eddy diffusivities ($10^4 \text{ m}^2 \text{ s}^{-1}$) at 275–400 m during the time periods (a) June 1994 to May 1995, (b) June 1995 to May 1996, (c) June 1996 to May 1997 and (d) June 1997 to May 1998. Black contours are barotropic streamlines ψ_g defined in equation (1). The thick green lines are contours corresponding to 1500 m, 3000 m, and 4500 m topography. The hatched areas indicate regions where the eddy diffusivity estimates are indistinguishable from zero at the 95% confidence level. Methods to estimate the error bar of these diffusivities are described by *Chen et al.* [2014].

the intense KE jet and becomes elevated within the weak KE jet (Figure 6). Mixing theories, based on homogeneity and linear assumptions, suggest that if the eddy propagation speed along the mean flow direction matches the mean flow magnitude, cross-jet mixing is elevated; on the other hand, if the eddy propagation speed differs from the mean flow magnitude, cross-jet mixing can be suppressed [e.g., *Green, 1970; Ferrari and Nikurashin, 2010; Chen et al., 2015*] (section 1). In the KE region, the mean flow suppresses mixing within the intense jet area away from topography [*Chen et al., 2014*]. These theories indicate that the spatial structure of mixing should be influenced by the mean flow and eddy velocity magnitude, and thus the two states of the KE. During periods 1 and 2, the jet is intense west of 150°E . Consistently, in spite of the large eddy velocity magnitude within the KE jet, mixing is small within the KE jet west of 150°E . During period 3, when the jet is weak and contracted, mixing is large within the weak KE jet east of the Izu Ridge. Consistent with these theories, mixing in period 4 is relatively small due to both the intense KE jet and relatively small eddy velocity magnitude (Figures 1d, 2d, and 6).

4.1.2. Deep Ocean

Compared to upper-ocean eddy diffusivities, deep-ocean eddy diffusivities, i.e., those below 1900 m, have less temporal variability (Figure 7). In all four periods, elevated mixing occurs at 150°E inside the jet, east of the Izu Ridge south of the jet, and at some scattered spots east of the Shatsky Rise. Because diffusivities vary with depth and location, to quantitatively assess the magnitude of diffusivity anomalies relative to the time-mean diffusivity, we define an index

$$\Pi[\mathbf{x}, (T_1, T_2)] = \left| \frac{\kappa_{\perp}[\mathbf{x}, (T_1, T_2)] - \overline{\kappa_{\perp}}(\mathbf{x})}{\overline{\kappa_{\perp}}(\mathbf{x})} \right|, \quad (5)$$

where $\overline{\kappa_{\perp}}$ denotes the temporal average of cross-stream eddy diffusivities over the entire 4 year time period (June 1994 to May 1998) and $\kappa_{\perp}[\mathbf{x}, (T_1, T_2)]$ denotes the cross-stream eddy diffusivities in each time period $[T_1, T_2]$ at position \mathbf{x} . We diagnosed Π at each depth level over each time period and in the domain $130^\circ - 165^\circ\text{E}$, $28^\circ - 40^\circ\text{N}$, and then performed an average over the four time periods and the entire domain. The index averaged over the upper 900 m reaches 2.0, but the index averaged below 900 m is only 0.8. This result indicates that mixing in the deep ocean has less temporal variability.

The relatively small temporal variability of mixing in the deep ocean is consistent with the deep ocean's small temporal variability of both eddy kinetic energy and mean flow. Theory suggests that both the mean flow and eddies influence mixing rates [e.g., *Ferrari and Nikurashin, 2010; Chen et al., 2015*]. Figure 8 shows the eddy velocity magnitude, and Figure 9 shows mean flow patterns in the four study periods. Eddy velocity magnitude is large at $145^\circ - 155^\circ\text{E}$ in the KE jet in all four periods. Consistently throughout the four periods, the time-mean circulation in POP indicates anticyclonic circulation east of the Izu Ridge near the Japan

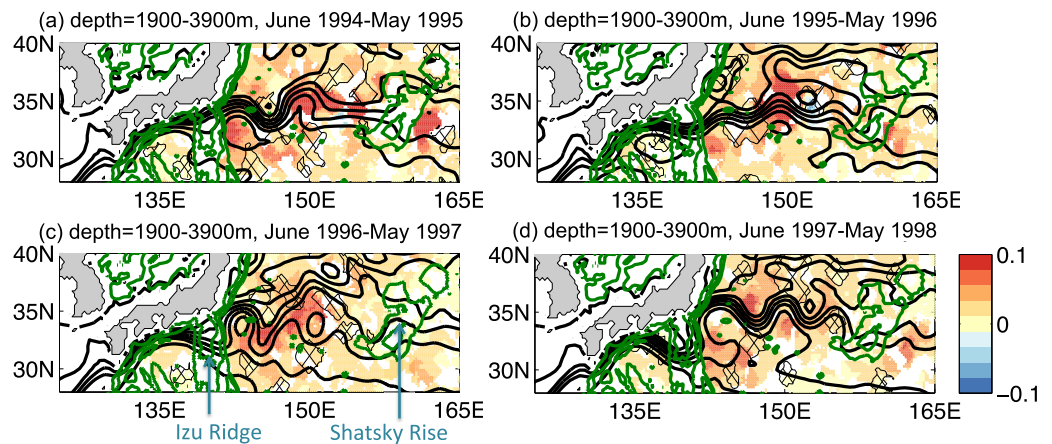


Figure 7. Same as Figure 6, but for the depth range 1900–3900 m. The upper 3900 m is divided into 11 depth ranges for the diffusivity estimation, and diffusivities at the 8th–11th depth ranges were averaged together to produce this figure.

coast, as reported by *Jayne et al.* [2009], and cyclonic circulation at the jet near 150°E, which is consistent with KESS observations [*Greene et al.*, 2009] (Figure 9).

The persistence of anticyclonic and cyclonic structures below 1900 m shown in Figure 9 contributes to the small temporal variability of mixing at the same depth range. The persistence of these circulation structures could be due to the fact that the deep ocean, isolated from atmospheric forcing, is largely topographically controlled. The anticyclone could be induced by the seamounts located at the anticyclone center. As summarized by *Greene et al.* [2009], the trapping of anticyclonic circulation over seamounts can be explained using the Taylor-Proudman theorem and equilibrium statistical mechanics. The anticyclone could also be the manifestation of the recirculation gyre often identified in the upper ocean [*Jayne et al.*, 2009]. The persistence of cyclonic circulation near 150°E could be due to the interaction of synoptic eddies with seamounts located at 140°–150°E [*Greene et al.*, 2009]. Though the lower-layer stretching due to the meandering of the upper-ocean jet has been confirmed to be responsible for the deep cyclone generation under Gulf Stream troughs [*Savidge and Bane*, 1999], this mechanism plays a minor role in the KE system [*Greene et al.*, 2009]. Further discussion of the mean flow patterns is beyond the scope of this study.

At middepth (900–1900 m), the horizontal patterns of eddy diffusivities have similarities to both upper ocean and deep ocean structures. For example, elevated mixing occurs east of the Izu Ridge, at some spots near the Shatsky Rise and downstream of the KE jet, where it has weakened (not shown). At 400–900 m, the

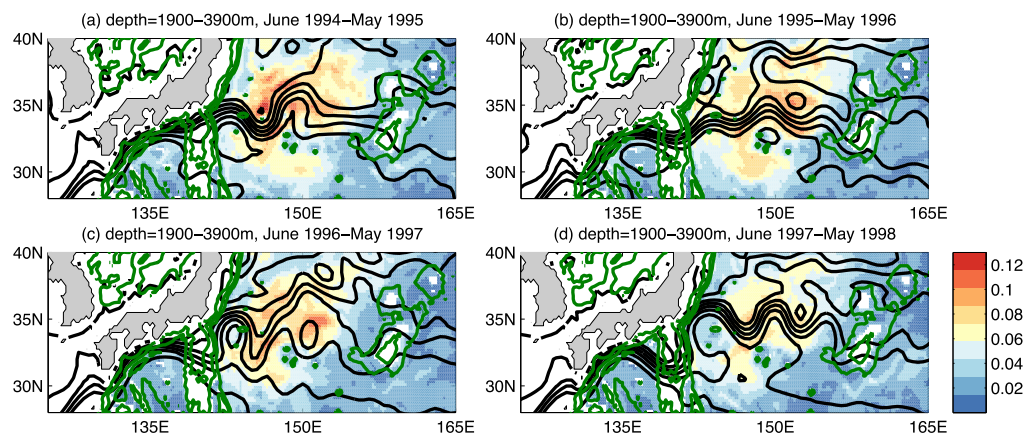


Figure 8. The vertical average of the time-mean eddy velocity magnitude (color, m/s) over the depth range 1900–3900 m for (a) June 1994 to May 1995, (b) June 1995 to May 1996, (c) June 1996 to May 1997 and (d) June 1997 to May 1998. Black contours indicate the barotropic streamlines ψ_g . The dark green lines are contours corresponding to 1500 m, 3000 m, and 4500 m topography. As described in the caption of Figure 1, eddy velocity denotes the deviation of total velocity from its time-mean over the selected time period.

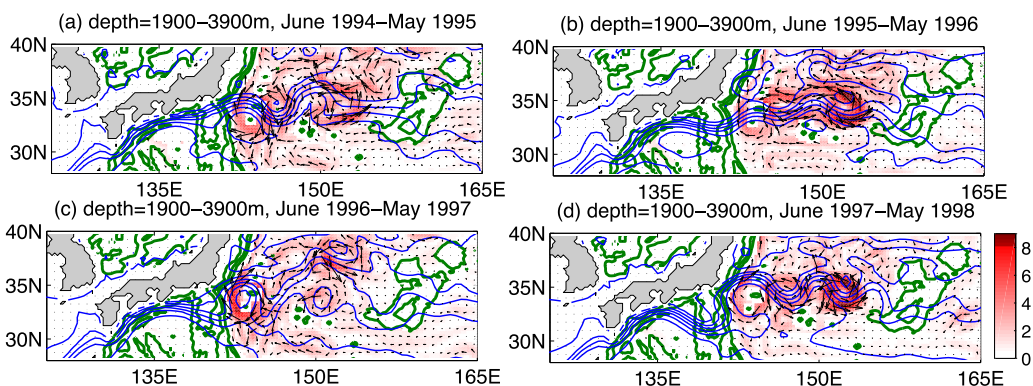


Figure 9. The vertical average of the time-mean velocity over the depth range 1900–3900 m for (a) June 1994 to May 1995, (b) June 1995 to May 1996, (c) June 1996 to May 1997 and (d) June 1997 to May 1998. Color shows the velocity magnitude (cm s^{-1}), and the vector represents its direction. Blue contours indicate barotropic streamlines and dark green lines are topography contours.

horizontal structures of eddy diffusivities are similar to the diffusivity patterns at 275–400 m (Figure 6). The vertical coherence of diffusivity structures in the upper 900 m is consistent with the vertical coherence of the KE jet and its associated eddy field in this depth range.

4.2. Cross-Jet Mixing Within the KE Jet

We now evaluate the magnitudes of cross-stream diffusivities within the KE jet and their impact on inter-gyre exchange.

4.2.1. Magnitudes of Total Mixing Across the KE Jet

Because mixing within the KE jet in the stable and unstable states has complex longitudinal variability, we assess whether the magnitude of total cross-jet mixing within the KE jet differs between the two states. We define the KE jet area as the area centered around the KE path at its center and extending northward and southward from this location by one degree (Figure 10). One method to estimate cross-jet mixing averaged within the KE jet is to average eddy diffusivities in adaptive bins with centroids located within the KE jet. However, some of the adaptive bins with centroids within the KE jet also encompass regions outside of the KE jet. Therefore, we estimated total cross-jet mixing within the KE jet from equation (3) by treating the KE jet area as one large bin and taking advantage of all the pseudo tracks located within the KE jet area at their center time, i.e., $\tau = 0$.

Using the large bin approach, we obtained eddy diffusivities averaged within the KE jet at 130° – 165°E during each time period (Figure 11a). One might hypothesize that the mixing rate should be larger in the unstable state because of the weakened KE jet, leading to less mixing suppression, and because of heightened eddy activity. However, Figure 11a shows that, at 125–900 m and 1400–2400 m, eddy diffusivities in

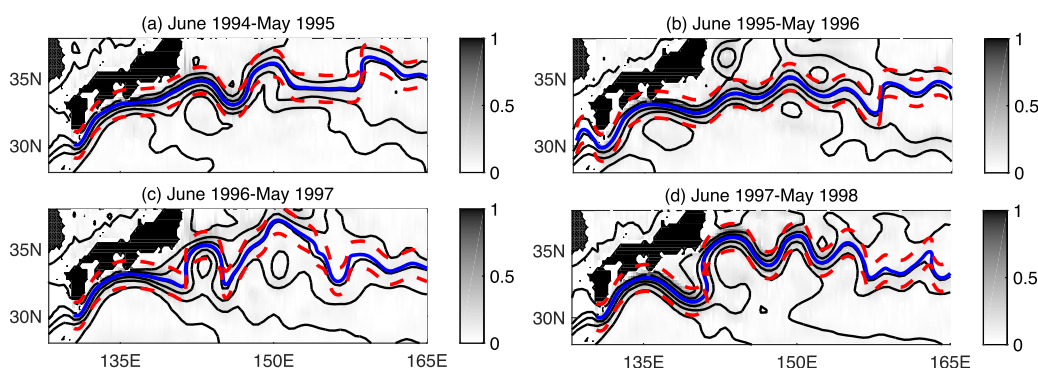


Figure 10. Normalized absolute value of $f^{-1} \partial \eta / \partial y$, where η is the time-mean sea surface height over the time period (a) June 1994 to May 1995, (b) June 1995 to May 1996, (c) June 1996 to May 1997 and (d) June 1997 to May 1998. The solid blue curve indicates the KE path center, which corresponds to the 70 cm SSH and is very close to the maximum $|f^{-1} \partial \eta / \partial y|$ at each longitude. The red lines, locating north and south of the path center by one degree, are assumed to be the KE jet boundary. The area inside the red lines is considered to be inside the KE jet.

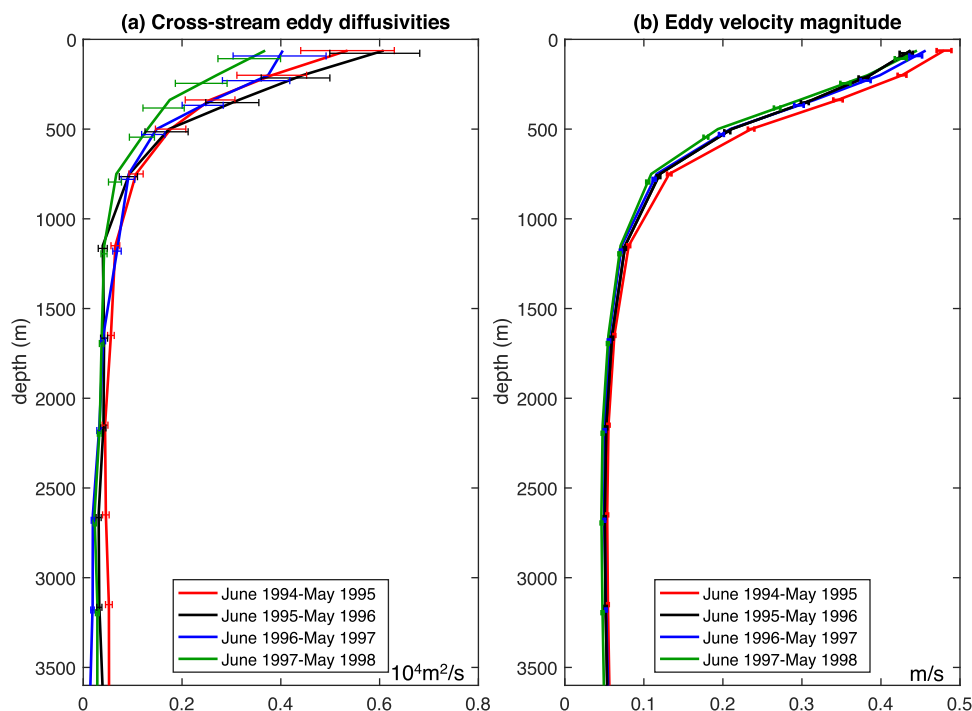


Figure 11. (a) Cross-stream eddy diffusivities and (b) eddy velocity magnitude averaged over the area within the KE jet at 130° – 165° E in each time period. Error bars show uncertainties at 95% confidence level inferred from bootstrapping. Error bars are slightly displaced in depth to facilitate visual comparison.

period 3, which is an unstable state, are indistinguishable at the 95% confidence level from those in period 2, which is a stable state. Actually, eddy diffusivities in period 3 are statistically significantly larger than those in period 2 only at 900–1400 m. Period 3, a typical unstable state, does not systematically support more cross-jet mixing than period 2, a typical stable state. Our counterintuitive result can be attributed to two factors. First, eddy velocity magnitudes within the KE jet in periods 2 and 3 are indistinguishable from each other at most depth ranges (Figure 11b). Second, mixing in the stable state can be large in the downstream KE jet, which is weak and covers a broad longitude range (Figure 6b). Eddy diffusivities averaged within the KE jet in period 1 are statistically significantly larger than those in period 4 at all depth levels. We repeated the calculation over the longitude range of 130° – 155° E, and found that the basic features do not change: mixing and eddy activity all decay with depth; and period 3, the typical unstable year, does not correspond to maximum cross-jet mixing.

To quantify the variations of κ_{\perp} and u_{rms} relative to their means within the 4 year period, we defined an index similar to equation (5):

$$\tilde{\Pi}[z, (T_1, T_2)] = \left| \frac{a[z, (T_1, T_2)] - \bar{a}(z)}{\bar{a}(z)} \right|, \quad (6)$$

where a is an arbitrary variable as a function of depth z and time period $[T_1, T_2]$. For example, a can be κ_{\perp} or u_{rms} averaged within the KE jet. Here \bar{a} denotes the time-mean a over the 4 year period. Equation (6) essentially replaces κ_{\perp} in equation (5), which has both three-dimensional spatial variation and temporal variation, by the arbitrary variable a , which only varies with depth and the time period. Note that $\tilde{\Pi}[z, (T_1, T_2)]$ is a function of depth z and time period $[T_1, T_2]$. Thus, the average of $\tilde{\Pi}[z, (T_1, T_2)]$ over the four time periods (periods 1–4) is only a function of z , and the range of its values for selected variables are shown in Table 1. For κ_{\perp} averaged over 130° – 165° E within the KE jet, the average of $\tilde{\Pi}$ over periods 1–4 varies from 0.1 to 0.4, and for u_{rms} averaged over the same area, it ranges from 0.03 to 0.06 (Table 1). These results imply that u_{rms} averaged over this area is comparatively steady relative to κ_{\perp} averaged over the same area.

4.2.2. Implications for Eddy Flux Parameterization

We have described the spatiotemporal structures of eddy mixing rates in the KE region. Next, we discuss the implications of the mixing results presented above for the parameterization of eddy heat fluxes, which

Table 1. The Average of $\bar{\Pi}[z, (T_1, T_2)]$ Over the Four Time Periods (Periods 1–4) in the POP Model for Eddy Velocity Magnitude u_{rms} , Cross-Stream Eddy Diffusivities κ_{\perp} , Total Eddy Heat Fluxes and Time-Mean Temperature Gradient Across the KE Jet, and for Total Eddy Salt Fluxes and Time-Mean Salinity Gradient Across the KE Jet^a

Variables Used to Compute $\bar{\Pi}$	$\bar{\Pi}$
u_{rms} averaged over 130°–165° E within the KE jet	0.03–0.06
κ_{\perp} averaged over 130°–165° E within the KE jet	0.1–0.4
Total eddy heat fluxes across the KE jet at 130°–165° E below 125 m	0.4–2
Time-mean temperature gradient across the KE jet at 130°–165° E	0.1–0.2
Total eddy salt fluxes across the KE jet at 130°–165° E below 125 m	0.3–2
Time-mean salinity gradient across the KE jet at 130°–165° E	0.1–0.2

^aNote that $\bar{\Pi}[z, (T_1, T_2)]$, defined in equation (6), is a function of depth z and time period $[T_1, T_2]$. Therefore, the average of $\bar{\Pi}$ over the four time periods is a function of depth z , and thus it has a range of values for each variable, as shown in the table.

are large in the KE region compared to the open ocean. Eddy heat transport in the western boundary current region (e.g., the KE region) is strong [e.g., Stammer, 1998; Wunsch, 1999; Jayne and Marotzke, 2002; Volkov et al., 2008]. Consistently, during our study period, in the POP model, the total eddy heat fluxes across the KE jet at 130°–165° E are approximately 11 times greater than the net poleward eddy flux in the quiescent northeast Pacific (33°N, 165°–250°E). The corresponding ratio for eddy salt fluxes is approximately 160, an order of magnitude greater than the heat flux ratio. These results confirm the important role of the KE in inter-gyre exchange and indicate that

the representation of eddy tracer fluxes across the KE is likely to be important for coarse resolution climate models.

The inter-annual variability of cross-jet eddy fluxes within the KE jet is significant in POP: below 125 m, the average of $\bar{\Pi}$ over periods 1–4 for cross-jet eddy heat flux varies from 0.4 to 2, and it varies from 0.3 to 2 for cross-jet eddy salt fluxes (Table 1). We assume that

$$\overline{v'_{\perp} c'} = \kappa_{\perp} \frac{d\bar{c}}{dy_n}, \tag{7}$$

where c is tracer concentration (either salinity or temperature in this case), $\overline{v'_{\perp} c'}$ is cross-jet eddy tracer flux and $d\bar{c}/dy_n$ is cross-jet tracer gradient. For κ_{\perp} averaged within the KE jet, the average of $\bar{\Pi}$ over periods 1–4 ranges from 0.1 to 0.4 (Table 1). For $d\bar{c}/dy_n$, i.e., cross-jet temperature and salinity gradient, averaged within the KE jet, it varies from 0.1 to 0.2 (Table 1). These results show that the inter-annual variability of both κ_{\perp} and $d\bar{c}/dy_n$ contribute significantly to the inter-annual variability of cross-jet eddy tracer fluxes in the KE region, implying that, to represent eddy transport correctly, the time-dependence of eddy mixing coefficients should be included in coarse-resolution climate models.

One caveat, however, is that, equation (7) is based on two assumptions: spatial homogeneity and consistency between Eulerian and Lagrangian eddy diffusivities. First, the Green's function approach suggests that the accurate form of the eddy fluxes $\overline{v'_{\perp} c'}$ is a function of both local and nonlocal mean tracer gradients [e.g., Kraichnan, 1987; Chen et al., 2015]. If the system is approximately spatially homogeneous, the accurate form of $\overline{v'_{\perp} c'}$ [Chen et al., 2015, equation (B5)] reduces to the standard formula of eddy parameterization,

$$\overline{v'_{\perp} c'} = \kappa_{\perp}^E \frac{d\bar{c}}{dy_n}, \tag{8}$$

where κ^E is the Eulerian cross-stream eddy diffusivities. Second, assuming that the Lagrangian eddy diffusivities presented in this paper are consistent with the Eulerian eddy diffusivities, κ^E , converts equation (8) to equation (7). Davis [1991] provides more detail on the validity of equation (7). Another caveat is that our discussion of the implications of our Table 1 results is based on the assumption that equation (7) holds for the spatially averaged eddy tracer fluxes, cross-jet tracer gradient and eddy diffusivities.

5. Discussion and Conclusion

The KE jet transitions between stable and unstable states on interannual time scales. Though the mechanisms governing the two states have been studied previously, the impact of the two KE states on the ocean and climate system has received less attention. This study evaluates how cross-KE isopycnal mixing differs in the stable and unstable states. Isopycnal eddy diffusivities across the mean flow direction were estimated

using numerical particles deployed in a global eddying numerical model (POP) at nominal 0.1° resolution. Model-data comparisons show that the model captures the amplitude of KE path variability at the resolved frequencies (Figure 5). We focus on the time period from June 1994 through May 1998, which covers a representative stable state, unstable state and the state transition period.

The two states of the KE paths contribute to the temporal variability of mixing structures in the upper ocean, which are influenced both by mean flow and eddy strengths. Mixing is similar in the two states: upstream of the KE jet, where the KE jet is intense, upper-ocean diffusivities are generally smaller within the jet than outside the jet; downstream, where the flow is weak, upper-ocean diffusivities are generally large within the KE jet. The differences in the KE jet structure and strengths between the two states lead to differences in mixing structures. During June 1995 to May 1996, a typical stable state period, the KE jet is intense west of 150°E and thus upper-ocean mixing is elevated east of 150°E . However, during June 1996 to May 1997, a typical unstable state period, the KE jet is weak in the longitude range west of 150° and east of the Izu Ridge, and thus mixing is elevated west of 150°E . In the deep ocean, the broad structures of diffusivities have less temporal variability. They are generally large east of the Izu Ridge, where an anticyclonic circulation occurs, and near 150°E , where there is persistent cyclonic circulation, and at some scattered spots along the Shatsky Rise.

The variable κ_\perp averaged over $130^\circ - 165^\circ\text{E}$ within the KE jet differs from its time mean by 10%-40%. This is because the variable $\bar{\Gamma}$ for κ_\perp averaged over $130^\circ - 165^\circ\text{E}$ within the KE jet, which is defined in equation (6) and used to quantify the temporal variability, is 0.1–0.4 (section 4.2.1; Table 1). Therefore, the temporal variability of eddy mixing across the KE jet is noticeable, indicating the need for time-dependent eddy mixing coefficients in coarse-resolution models (section 4.2.2). Since coarse-resolution models are still used routinely, particularly for centennial-scale climate simulations, there would be value in quantifying the interannual variability of mixing in the global ocean, and in formulating mixing parameterizations to account for time-dependence.

In spite of the noticeable temporal variability of κ_\perp averaged over $130^\circ - 165^\circ\text{E}$ within the KE jet, cross-jet mixing during June 1996 to May 1997 (a typical unstable state) is statistically indistinguishable from that during June 1995 to May 1996 (a typical stable state) at all the depths except 900–1400 m (Figure 11a). This counterintuitive result can be attributed to two causes. First, in both time periods, there is elevated mixing in the weakened downstream part of the KE jet, although the longitude ranges of this elevated mixing differ in the two time periods. Second, eddy velocity magnitudes averaged within the KE jet in the two time periods are also indistinguishable (Figure 11b).

This study is the first effort to compare isopycnal mixing in the stable and unstable states of the Kuroshio Extension. Given the computation demand of global simulations with online numerical floats, this study only covers a 4 year period and thus results presented here only cover one representative stable state, unstable state and the state transition period. Therefore, our results cannot be interpreted as the climate-mean mixing estimates for the stable state and for the unstable state. As shown in Figure 4 and by *Qiu and Chen* [2010], there is much temporal variability of flow properties (e.g., EKE, path length, path positions) even within the stable-state period or unstable-state period (Figure 4) [*Qiu and Chen*, 2010]. Thus, we speculate that the spatial structure and magnitude of eddy diffusivities also have strong temporal variability within the stable-state or unstable-state periods.

However, our results based on the four numerical experiments are still illuminating. First, the strong spatio-temporal eddy diffusivity variability revealed in this study indicates the need to use spatially and temporally varying mixing coefficients in coarse-resolution climate models. Second, in the 4 year periods we examined, consistent with mixing theories, the upper-ocean eddy mixing structures are due to the combined effects of the mean flow and eddies, whose magnitude and broad spatial structures oscillate between the stable and unstable states. Third, regardless of the state of the KE system, strong mixing in the upper ocean in the 4 years that we examined occurs in the downstream KE jet, where the jet is weak and eddy activity is strong.

Our estimates can be further improved. First, one can extend the mixing estimation from 4 years to a much longer time period, which would allow us to obtain the climate-mean mixing patterns for the stable state and unstable state. Second, besides the float-based mixing estimation method employed here, quite a few other methods exist, such as effective diffusivities [*Nakamura*, 1996] and tracer-based least-square estimates [*Bachman et al.*, 2015; *Lu et al.*, 2016]. Though there is previous evidence regarding the consistency of

mixing diagnosis methods in certain cases [e.g., *Klocker et al.*, 2012b; *Abernathey et al.*, 2013], the sensitivity of the results presented in this study to the choice of mixing estimation approach and model configuration should be assessed. Third, this study focuses on cross-stream eddy diffusivities, as the cross-stream component within the jet is relevant to the exchange of tracers between subtropical and subpolar gyres. Estimating the full diffusivity tensor would also be of value [e.g., *Rypina et al.*, 2012; *Abernathey et al.*, 2013; *Bachman and Fox-Kemper*, 2013; *Wolfram et al.*, 2015; *Kamenkovich et al.*, 2015]. The methodology used in this study could also be employed to investigate mixing in other western boundary current systems, such as the Gulf Stream.

Though the KE and Southern Ocean jets are visually similar, eddy diffusivities averaged within the KE and Southern Ocean jets have different vertical structures. *Abernathey et al.* [2010] estimated the vertical structure of circumpolar-averaged effective diffusivities across the Southern Ocean jet, and found that there is a local maximum of diffusivities at around 1000 m within the jet core. The diffusivities averaged within the KE jet, however, decay with depth in all the 4 year periods, as do eddy velocity magnitudes averaged within the KE jet (Figure 11). Additionally, the longitude-depth cross section of eddy diffusivities has strong longitudinal variation in both regions [e.g., *Griesel et al.*, 2014; *Chen et al.*, 2014]. *Abernathey et al.* [2010] hypothesized that the middepth maximum of mixing in the Southern Ocean is due to the effect of a critical layer, where the eddy phase speed along the mean flow direction matches the mean flow magnitude. *Chen et al.* [2014] found that, a critical layer is absent within the intense KE jet, which is consistent with the lack of a middepth maximum of cross-jet mixing within the KE jet. The critical layer theory represents a special case of the more generalized mean flow suppression theory by *Killworth* [1997] and *Ferrari and Nikurashin* [2010]. An additional caveat is that these theories are based on linear and homogeneous assumptions [*Chen et al.*, 2015]. Therefore, although they have some skill representing mixing, they are not valid everywhere in the ocean. For example, in the KE region, they are only valid in the intense KE jet region away from topography [*Chen et al.*, 2014]. These theories also cannot capture the vertical structure of observed eddy diffusivities in the upper 1000 m west of the Drake Passage in the Southern Ocean [*Bates et al.*, 2014]. A parameterization capable of capturing the vertical structure of diffusivities especially for the highly nonlinear regime is needed (P. Wolfram, personal communication, 2016).

This work complements the KESS field campaign, which aimed to evaluate eddy generation and cross-frontal eddy fluxes [e.g., *Donohue et al.*, 2008]. The KESS observing array was mesoscale resolving and was located in the region of highest eddy kinetic energy in the KE (143°–148°E, 32°–37°N) for a 16 month time period; during this time it captured a transition from a stable to unstable state [*Bishop et al.*, 2013; *Bishop*, 2013]. Using the tracer-based least-square estimation approach of *Lu et al.* [2016], one would be able to estimate eddy diffusivities using velocity and temperature observations from KESS. Our work provides mixing estimates in the two states in a much larger spatial domain.

Acknowledgments

This work was supported by the National Science Foundation (OCE0850463, OCE0960914, and OCE1234473). JLM and STG were also supported by DOE/Office of Science grant DE-SC0014440. JLM was also supported by DOE/Office of Science grant DE-SC0012778 and via a Los Alamos National Laboratory subcontract. Elena Yulaeva provided the interpolated atmospheric forcing fields for the numerical experiments. We also benefited from discussions with Alexa Griesel about the float deployment strategy. Insightful comments from Phillip J. Wolfram and an anonymous reviewer greatly improved the manuscript. Numerical output from these experiments is stored at the National Center for Computational Sciences. Computational resources for the model run were provided by NSF XSEDE Resource Grant TG-OCE130018. The altimeter product used in section 3 was produced and distributed by AVISO (<http://www.aviso.altimetry.fr/>), as part of the Ssalto ground processing segment.

References

- Abernathey, R., J. Marshall, M. Mazloff, and E. Shuckburgh (2010), Enhanced isopycnal mixing at steering levels in the Southern Ocean, *J. Phys. Oceanogr.*, *40*, 170–184.
- Abernathey, R., D. Ferreira, and A. Klocker (2013), Diagnostics of eddy mixing in a circumpolar channel, *Ocean Modell.*, *72*, 1–16.
- Bachman, S., and B. Fox-Kemper (2013), Eddy parameterization challenge suite I: Eady spindown, *Ocean Modell.*, *64*, 12–28.
- Bachman, S., B. Fox-Kemper, and F. Bryan (2015), A tracer-based inversion method for diagnosing eddy-induced diffusivity and advection, *Ocean Modell.*, *86*, 1–14.
- Bates, M., R. Tulloch, J. Marshall, and R. Ferrari (2014), Rationalizing the spatial distribution of mesoscale eddy diffusivity in terms of mixing length theory, *J. Phys. Oceanogr.*, *44*(6), 1523–1540.
- Bishop, S. P. (2013), Divergent eddy heat fluxes in the Kuroshio Extension at 144°–148°E. Part ii: Spatiotemporal variability, *J. Phys. Oceanogr.*, *43*(11), 2416–2431.
- Bishop, S. P., D. R. Watts, and K. A. Donohue (2013), Divergent eddy heat fluxes in the Kuroshio Extension at 144°–148°E: Part 1: Mean structure, *J. Phys. Oceanogr.*, *43*, 1533–1550.
- Bishop, S. P., F. O. Bryan, and J. R. Small (2015), Bjerknes-like compensation in the wintertime north Pacific, *J. Phys. Oceanogr.*, *45*(5), 1339–1355.
- Boland, E. J. D., E. Shuckburgh, P. H. Haynes, J. R. Ledwell, M. J. Messias, and A. J. Watson (2015), Estimating a submesoscale diffusivity using a roughness measure applied to a tracer release experiment in the Southern Ocean, *J. Phys. Oceanogr.*, *45*(6), 1610–1631.
- Chelton, D. B., M. G. Schlax, and R. M. Samelson (2011), Global observations of nonlinear mesoscale eddies, *Prog. Oceanogr.*, *91*, 167–216.
- Chen, R., J. L. McClean, S. T. Gille, and A. Griesel (2014), Isopycnal eddy diffusivities and critical layers in the Kuroshio Extension from an eddy ocean model, *J. Phys. Oceanogr.*, *44*(8), 2191–2211.
- Chen, R., S. T. Gille, J. L. McClean, G. R. Flierl, and A. Griesel (2015), A multi-wavenumber theory for eddy diffusivities and its application to the southeast Pacific (DIMES) region, *J. Phys. Oceanogr.*, *45*(7), 1877–1896.
- Chiswell, S. M. (2013), Lagrangian time scales and eddy diffusivity at 1000 m compared to the surface in the South Pacific and Indian Oceans, *J. Phys. Oceanogr.*, *43*(12), 2718–2732.

- Danabasoglu, G., and J. Marshall (2007), Effects of vertical variations of thickness diffusivity in an ocean general circulation model, *Ocean Modell.*, *18*, 122–141.
- Davis, R. (1987), Modelling eddy transport of passive tracers, *J. Mar. Res.*, *45*, 635–666.
- Davis, R. (1991), Observing the general circulation with floats, *Deep Sea Res., Part A*, *38*, suppl. 1, S531–S571.
- Delman, A. S., J. L. McClean, J. Sprintall, L. D. Talley, E. Yulaeva, and S. R. Jayne (2015), Effects of eddy vorticity forcing on the mean state of the Kuroshio Extension, *J. Phys. Oceanogr.*, *45*(5), 1356–1375.
- Donohue, K., et al. (2008), Program studies of the Kuroshio extension, *Eos Trans. AGU*, *89*, 161–162.
- Douglass, E. M., S. R. Jayne, F. O. Bryan, S. Peacock, and M. Maltrud (2012), Kuroshio pathways in a climatologically forced model, *J. Oceanogr.*, *68*(5), 625–639.
- Dukowicz, J. K., and R. D. Smith (1994), Implicit free-surface method for the Bryan-Cox- Semtner ocean model, *J. Geophys. Res.*, *99*, 7991–8014.
- Ferrari, R., and M. Nikurashin (2010), Suppression of eddy diffusivity across jets in the Southern Ocean, *J. Phys. Oceanogr.*, *40*, 1501–1519.
- Gille, S. T., et al. (2012), The diapycnal and isopycnal mixing experiment: A first assessment, *CLIVAR Exch.*, *17*(1), 46–48.
- Green, J. S. A. (1970), Transport properties of the large-scale eddies and the general circulation of the atmosphere, *Q. J. R. Meteorol. Soc.*, *96*, 157–185.
- Greene, A. D., G. G. Sutyrin, and D. R. Watts (2009), Deep cyclogenesis by synoptic eddies interacting with a seamount, *J. Mar. Res.*, *67*, 305–322.
- Greene, A. D., D. R. Watts, G. G. Sutyrin, and H. Sasaki (2012), Evidence of vertical coupling between the Kuroshio Extension and topographically controlled deep eddies, *J. Mar. Res.*, *70*, 719–747.
- Griesel, A., S. T. Gille, J. Sprintall, J. L. McClean, J. H. LaCasce, and M. E. Maltrud (2010), Isopycnal diffusivities in the Antarctic Circumpolar Current inferred from Lagrangian floats in an eddying model, *J. Geophys. Res.*, *115*, C06006, doi:10.1029/2009JC005821.
- Griesel, A., J. McClean, S. Gille, J. Sprintall, and C. Eden (2014), Eulerian and lagrangian isopycnal eddy diffusivities in the southern ocean of an eddying model, *J. Phys. Oceanogr.*, *44*(2), 644–661.
- Griesel, A., C. Eden, N. Koopmann, and E. Yulaeva (2015), Comparing isopycnal eddy diffusivities in the Southern Ocean with predictions from linear theory, *Ocean Modell.*, *94*, 33–45.
- Holmes, R., J. Moum, and L. Thomas (2016), Evidence for seafloor-intensified mixing by surface-generated equatorial waves, *Geophys. Res. Lett.*, *43*, 1202–1210, doi:10.1002/2015GL066472.
- Ito, T., and J. Marshall (2008), Control of lower-limb overturning circulation in the Southern Ocean by diapycnal mixing and mesoscale eddy transfer, *J. Phys. Oceanogr.*, *38*(12), 2832–2845.
- Jayne, S. R., and J. Marotzke (2002), The oceanic eddy heat transport, *J. Phys. Oceanogr.*, *32*(12), 3328–3345.
- Jayne, S. R., et al. (2009), The Kuroshio Extension and its recirculation gyres, *Deep Sea Res., Part I*, *56*, 2088–2099.
- Kamenkovich, I., I. I. Rypina, and P. Berloff (2015), Properties and origins of the anisotropic eddy-induced transport in the North Atlantic, *J. Phys. Oceanogr.*, *45*(3), 778–791.
- Katsumata, K., and H. Yoshinari (2010), Uncertainties in global mapping of Argo drift data at the parking level, *J. Oceanogr.*, *66*(4), 553–569.
- Kawabe, M. (1986), Transition processes between the three typical paths of the Kuroshio, *J. Oceanogr. Soc. Jpn.*, *42*(3), 174–191.
- Killworth, P. D. (1997), On the parameterization of eddy transfer. Part 1: Theory, *J. Mar. Res.*, *55*, 1171–1197.
- Klocker, A., R. Ferrari, and J. H. LaCasce (2012a), Estimating suppression of eddy mixing by mean flows, *J. Phys. Oceanogr.*, *42*, 1566–1576.
- Klocker, A., R. Ferrari, J. H. LaCasce, and S. Merrifield (2012b), Reconciling float-based and tracer-based estimates of eddy diffusivities, *J. Mar. Res.*, *70*(4), 569–602.
- Koszalka, I. M., and J. H. LaCasce (2010), Lagrangian analysis by clustering, *Ocean Dyn.*, *60*(4), 957–972.
- Kraichnan, R. H. (1987), Eddy viscosity and diffusivity: Exact formulas and approximations, *Complex Syst.*, *1*(4–6), 805–820.
- LaCasce, J. H., and A. Bower (2000), Relative dispersion in the subsurface North Atlantic, *J. Mar. Res.*, *58*(6), 863–894.
- LaCasce, J. H., R. Ferrari, J. Marshall, R. Tulloch, D. Balwada, and K. Speer (2014), Float-derived isopycnal diffusivities in the DIMES experiment, *J. Phys. Oceanogr.*, *44*(2), 764–780.
- Lin, P., F. Chai, H. Xue, and P. Xiu (2014), Modulation of decadal oscillation on surface chlorophyll in the Kuroshio Extension, *J. Geophys. Res. Oceans*, *119*, 187–199, doi:10.1002/2013JC009359.
- Lu, J., F. Wang, H. Liu, and P. Lin (2016), Stationary mesoscale eddies, up-gradient eddy fluxes and the anisotropy of eddy diffusivity, *Geophys. Res. Lett.*, *43*, 743–751, doi:10.1002/2015GL067384.
- Marshall, J., E. Shuckburgh, H. Jones, and C. Hill (2006), Estimates and implications of surface eddy diffusivity in the Southern Ocean derived from tracer transport, *J. Phys. Oceanogr.*, *36*, 1806–1821.
- Merrifield, S. T., L. S. Laurent, B. Owens, A. M. Thurnherr, and J. M. Toole (2016), Enhanced diapycnal diffusivity in intrusive regions of the Drake Passage, *J. Phys. Oceanogr.*, *46*(4), 1309–1321.
- Miyazawa, Y., X. Guo, and T. Yamagata (2004), Roles of mesoscale eddies in the Kuroshio paths, *J. Phys. Oceanogr.*, *34*(10), 2203–2222.
- Nakamura, N. (1996), Two-dimensional mixing, edge formation, and permeability diagnosed in an area coordinate, *J. Atmos. Sci.*, *53*, 1524–1537.
- Oh, I. S., V. Zhurbas, and W. Park (2000), Estimating horizontal diffusivity in the East Sea (Sea of Japan) and the northwest Pacific from satellite-tracked drifter data, *J. Geophys. Res.*, *105*, 6483–6492.
- Oka, E., and B. Qiu (2012), Progress of North Pacific mode water research in the past decade, *J. Oceanogr.*, *68*, 5–20.
- O'Reilly, C. H., and A. Czaja (2015), The response of the Pacific storm track and atmospheric circulation to Kuroshio Extension variability, *Q. J. R. Meteorol. Soc.*, *141*(686), 52–66.
- Qian, Y.-K., S. Peng, and Y. Li (2013), Eulerian and Lagrangian statistics in the South China Sea as deduced from surface drifters, *J. Phys. Oceanogr.*, *43*(4), 726–743.
- Qiu, B. (2003), Kuroshio Extension variability and forcing of the Pacific decadal oscillations: Responses and potential feedback, *J. Phys. Oceanogr.*, *33*(12), 2465–2482.
- Qiu, B., and S. Chen (2005), Variability of the Kuroshio Extension jet, recirculation gyre, and mesoscale eddies on decadal time scales, *J. Phys. Oceanogr.*, *35*, 2090–2103.
- Qiu, B., and S. Chen (2010), Eddy-mean flow interaction in the decadal modulating Kuroshio Extension system, *Deep Sea Res., Part II*, *57*, 1097–1110.
- Qiu, B., and S. Chen (2011), Effect of decadal Kuroshio Extension jet and eddy variability on the modification of North Pacific Intermediate Water, *J. Phys. Oceanogr.*, *41*, 503–515.
- Qiu, B., and W. Miao (2000), Kuroshio path variations south of Japan: Bimodality as a self-sustained internal oscillation, *J. Phys. Oceanogr.*, *30*(8), 2124–2137.

- Qiu, B., S. Chen, and P. Hacker (2007), Effect of mesoscale eddies on Subtropical Mode Water variability from the Kuroshio Extension System Study (KESS), *J. Phys. Oceanogr.*, *37*, 982–1000.
- Qiu, B., S. Chen, N. Schneider, and B. Taguchi (2014a), A coupled decadal prediction of the dynamic state of the Kuroshio Extension system, *J. Clim.*, *27*(4), 1751–1764.
- Qiu, B., S. Chen, P. Klein, H. Sasaki, and Y. Sasai (2014b), Seasonal mesoscale and submesoscale eddy variability along the North Pacific Subtropical Countercurrent, *J. Phys. Oceanogr.*, *44*(12), 3079–3098.
- Révelard, A., C. Frankignoul, N. Sennéchal, Y.-O. Kwon, and B. Qiu (2016), Influence of the decadal variability of the Kuroshio Extension on the atmospheric circulation in the cold season, *J. Clim.*, *29*(6), 2123–2144.
- Roach, C. J., D. Balwada, and K. Speer (2016), Horizontal mixing in the Southern Ocean from Argo float trajectories, *J. Geophys. Res. Oceans*, *121*, 5570–5586, doi:10.1002/2015JC011440.
- Rypina, I. I., I. Kamenkovich, P. Berloff, and L. Pratt (2012), Eddy-induced particle dispersion in the near-surface Atlantic, *J. Phys. Oceanogr.*, *42*, 2206–2228.
- Savidge, D. K., and J. M. Bane (1999), Cyclogenesis in the deep ocean beneath the Gulf Stream: 2 Dynamics, *J. Geophys. Res.*, *104*, 18,127–18,140.
- Stammer, D. (1998), On eddy characteristics, eddy transports, and mean flow properties, *J. Phys. Oceanogr.*, *28*(4), 727–739.
- Tracey, K. L., D. R. Watts, K. A. Donohue, and H. Ichikawa (2012), Propagation of Kuroshio Extension meanders between 143°E and 149°E, *J. Phys. Oceanogr.*, *42*, 581–601.
- Volkov, D. L., T. Lee, and L.-L. Fu (2008), Eddy-induced meridional heat transport in the ocean, *Geophys. Res. Lett.*, *35*, L20601, doi:10.1029/2008GL035490.
- Waterman, S. N., and S. R. Jayne (2011), Eddy-mean flow interaction in the along-stream development of a western boundary current jet: An idealized model study, *J. Phys. Oceanogr.*, *41*, 682–707.
- Waterman, S. N., N. G. Hogg, and S. R. Jayne (2011), Eddy-mean flow interaction in the Kuroshio Extension region, *J. Phys. Oceanogr.*, *41*, 1182–1208.
- Wolfram, P. J., T. D. Ringler, M. E. Maltrud, D. W. Jacobsen, and M. R. Petersen (2015), Diagnosing isopycnal diffusivity in an eddying, idealized midlatitude ocean basin via Lagrangian, in Situ, Global, High-Performance Particle Tracking (LIGHT), *J. Phys. Oceanogr.*, *45*(8), 2114–2133.
- Wunsch, C. (1999), Where do ocean eddy heat fluxes matter?, *J. Geophys. Res.*, *104*, 13,235–13,249.
- Zhurbas, V., and I. S. Oh (2003), Lateral diffusivity and Lagrangian scales in the Pacific Ocean as derived from drifter data, *J. Geophys. Res.*, *108*(C5), 3141, doi:10.1029/2002JC001596.
- Zhurbas, V., and I. S. Oh (2004), Drifter-derived maps of lateral diffusivity in the Pacific and Atlantic oceans in relation to surface circulation patterns, *J. Geophys. Res.*, *109*, C05015, doi:10.1029/2003JC002241.